Phonon dispersions of hydrogenated and dehydrogenated carbon nanoribbons

Megumi Yamada, Yoshihiro Yamakita, and Koichi Ohno
Department of Chemistry, Graduate School of Science, Tohoku University, Aramaki, Aoba-ku, Sendai 980-8578, Japan
(Received 29 May 2007; revised manuscript received 24 October 2007; published 13 February 2008)

Phonon dispersion relations are presented for carbon nanoribbons along multirow structures of hexagonal rings with zigzag and armchair edges. The dispersions are compared with the ΓK and ΓM dispersions of graphite as a function of ribbon width m. The force constants are obtained from zone folding for those of polycyclic aromatic hydrocarbons (PAHs) based on a transferable force-field model (MO/8 model). The vibrational mode patterns at the Γ point are calculated to be longitudinal or transverse in zigzag nanoribbons. All of the normal modes are categorized into the following four groups. (1) The acoustic branches which converge to the origin at Γ point allow estimation of the group velocity from their slopes. (2) The acoustic harmonics display systematic vibrational patterns with nonzero phase relations in the width direction. The number of nodes in amplitudes, $k=1-m$, represents dispersions in the width direction. (3) The optical branches which are commensurate with the multirow structures are optical fundamentals, whereas those incommensurate are optical harmonics. Both display systematic frequency changes with respect to the number of nodes (k) and ribbon widths (m). The optical harmonics of zigzag ribbons at Γ point shift in proportion to the inverse of ribbon width $1/m$, whereas the acoustic harmonics depend on $1/\sqrt{m}$. (4) The CH vibrations are less dispersive than these CC vibrations. The CH out-of-plane modes are characterized by strong infrared intensities, and their frequencies are calculated to be higher in zigzag ribbons than in armchair ribbons. This order is in line with the general tendencies for PAHs with solo and duo CH bonds. Hydrogenated and dehydrogenated nanoribbons are calculated to show similar phonon dispersions for their carbon networks. Phonon densities of states (DOSs) are compared between the nanoribbons and PAHs with particular shapes. Prominent DOS peaks are uniquely obtained for zigzag nanoribbons and linear PAHs at ~400 and 1400 cm^{-1}. Complete selection rules are given for the vibrational transitions in zigzag and armchair nanoribbons according to the irreducible representations for the primitive unit cells.

DOI: 10.1103/PhysRevB.77.054302 PACS number(s): 63.20.D−, 63.22.−m, 78.30.−j, 61.46.Fg

I. INTRODUCTION

The nanoscale structures of hexagonal sp^2 carbon networks, such as carbon nanotubes and graphene layers, have been studied extensively over the last decade. Structural determinations using transmission electron microscopy and scanning tunneling microscopy, and spatially resolved spectroscopy focusing on electronic and vibrational levels at particular positions have become possible.[1,2] The microfabrication of the nanoscale carbon networks has also been demonstrated using lithographic procedures[3] or voltages on a tips of scanning tunneling microscopes,[4] showing prospects for carbon-based electronics. In any carbon-based conductor, the motion of valence electrons will create significant changes in equilibrium structures and give rise to electron-phonon coupling (EPC). Therefore, the vibrational properties are of fundamental importance for electron transport in carbon-based conductors.

Upon going toward smaller structures, carbon networks will become close to molecules. The nanoscale materials are expected to possess the dual properties of infinite lattices and molecules. The Bloch theorem requires the wave functions to be periodic in an infinite lattice, whereas truncation in the translational symmetry imposes additional boundary conditions. As a result, chemical bonds and normal modes are affected by different conditions at inner and perimeter regions, though they could display significant periodicity along repeating structures. Indeed, the electronic and vibrational eigenstates have been found to be localized at the ends of carbon nanotubes[5,6] or at perimeters in large polycyclic aromatic hydrocarbons.[7,8] Thus, the physics of nanoscale systems cannot be described fully in reciprocal space, but descriptions accounting for particular molecular structures are required.

The vibrational wave functions of the crystal lattice are well characterized in reciprocal space by the wave vector. The phonons of graphite or carbon surfaces have been determined by wave-vector-sensitive experiments such as neutron scattering,[9] electron energy loss spectroscopy,[10–12] and inelastic x-ray scattering.[13] Optical determinations have also been performed by infrared[14] and Raman experiments.[14,15] Theoretical calculations for the phonon dispersions of graphite and nanotubes have been performed using force constant fitting,[15,16] tight-binding approximations,[17,18] and first-principles *ab initio* molecular orbital (MO) or density functional theory (DFT).[19–23] The problems found for these approaches include the fact that the available experimental data are limited to the simplest systems, and that the force-field parameters cannot be transferred between different carbon compounds.

The most primitive molecules comprising hexagonal carbon rings are polycyclic aromatic hydrocarbons (PAHs) and their dehydrogenated analogs (graphene). In particular, PAHs have been studied extensively by molecular spectroscopy experiments[24–29] and quantum chemical calculations. Semiempirical calculations and *ab initio* MO[30–34] or DFT[35,36] calculations have been performed so far, and compared with much experimental data. These theoretical approaches are in principle applicable to any nanoscale structure. Although

long computational times and convergence problems in the first-principles calculations limit the systems of interest to benchmark molecules, molecular-spectroscopic approaches can be performed extensively by employing semiempirical calculations. With careful comparisons with experiments, systematic tendencies for a number of PAHs can be investigated on the same theoretical basis. It is widely accepted that the vibrational properties of PAHs are governed by topological connections of the π electrons of six-membered rings. Therefore, it is of interest to study the nanoscale carbon materials with various ring topologies based on theoretical approaches connecting solid-state physics and molecular spectroscopy.

In this paper, we report on the phonon dispersions of carbon nanoribbons, which consist of one-dimensionally infinite, multirow structures of hexagonal rings. The electronic properties of carbon nanoribbons have been studied previously by tight-binding calculations,[17,18] and analogous ribbon structures have been grown experimentally on the TiC(755) surfaces.[37] However, vibrational properties are yet to be fully determined. We aim at establishing the phonon dispersions for carbon nanoribbons with zigzag and armchair edges using a force field model (MO/8 model) based on Hückel theory calculations.[38–42] This model incorporates effects from long-range interactions through bond-bond polarizabilities[43–47] and is applicable to any arbitrary PAH. It can also be extended to carbon nanotubes by adding curvature effects.[48,49] Therefore, the zone folding of the MO/8 force constants can give us direct connections between real PAHs and infinite systems. The widths of nanoribbons in the range of $m=1-20$ rings were studied for hydrogenated and dehydrogenated nanoribbons. We concentrate on the effects of the finite widths on vibrational mode patterns and transition intensities.

The main objectives discussed in this paper include the following. (a) Demonstrate the convergence behaviors for the dispersion curves of zigzag and armchair nanoribbons toward the phonons of graphite by increasing ribbon widths (Secs. III A and III D). (b) Calculate the evidence for systematic tendencies in vibrational mode patterns, especially the nodes of amplitudes in the width direction. Vibrational modes at the Γ point are classified into four groups. The G modes are compared with those of size-selected nanotubes[50] and theoretical data[16,19–23] (Secs. III B and III C). (c) Study the edge-localized modes in connection with infrared and Raman activities, and comparisons of the density of states between nanoribbons and PAHs with particular perimeters (Secs. III E–III G). (d) For completeness, computational details and optical selection rules are given in the Appendixes.

II. CALCULATIONS

The primitive lattice vectors $\boldsymbol{a}_1$ and $\boldsymbol{a}_2$ are defined for the hexagonal lattice, as shown in Fig. 1(a). It is commonly known that the helicity of carbon nanotubes is specified by coefficients for $\boldsymbol{a}_1$ and $\boldsymbol{a}_2$ in the chiral vector $\boldsymbol{C}_h$,[51,52]

$$\boldsymbol{C}_h = n_1\boldsymbol{a}_1 + n_2\boldsymbol{a}_2 = (n_1,n_2) \quad \{n_1,n_2\text{: integers}\}. \tag{1}$$

We define a carbon nanoribbon as a planar graphene which extends infinitely in the direction perpendicular to $\boldsymbol{C}_h$. Note

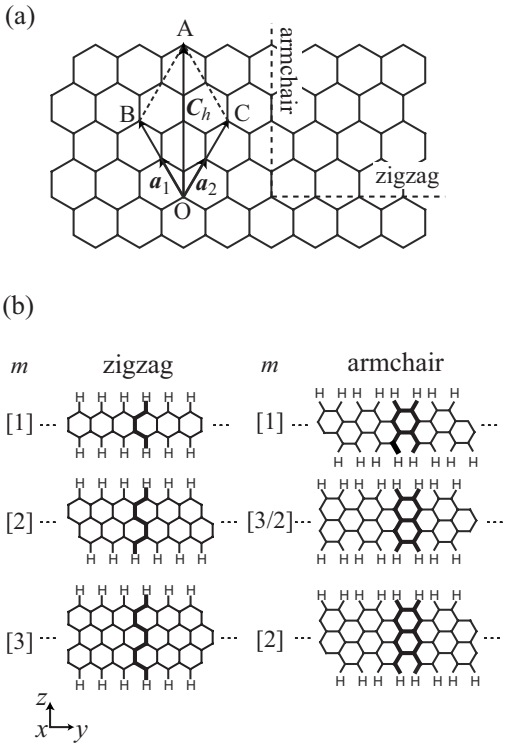

FIG. 1. Definitions for (a) primitive unit vectors $\boldsymbol{a}_1$ and $\boldsymbol{a}_2$ and (b) primitive unit cells (bold lines) for zigzag and armchair nanoribbons, respectively. Chiral vector $\boldsymbol{C}_h$ specifies the positions of carbon atoms that are located at edges in nanoribbons, or meet each other in nanotubes. $\boldsymbol{C}_h=(2,2)$ in this case. Ribbon width $[m]$ is equal to $2n$ for (n,n) zigzag ribbons and n for $(n,0)$ armchair ribbons, respectively.

that the carbon atoms at both ends of $\boldsymbol{C}_h$ are double counted in nanotubes since they coincide with each other. Table I presents relations between two special helicities for nanotubes and nanoribbons. The (n,n) and $(n,0)$ nanotubes are terminated by armchair and zigzag edges, respectively, whereas the nanoribbons that can be rolled up to form these nanotubes possess zigzag and armchair edges in the repeating direction, respectively. The perimeters of nanoribbons can be hydrogenated or dehydrogenated, and these are connected with PAHs and graphenes. The number of honeycomb rows is given by m in brackets (Table I), where m is equal to $2n$ or n in (n,n) zigzag or $(n,0)$ armchair ribbons, respectively. Figure 1(b) shows the primitive unit cells in nanoribbons by bold lines. The number of atoms in the unit is $2m+4$ in zigzag nanoribbons and $4m+8$ in armchair nanoribbons.

TABLE I. Representations for carbon nanotubes and nanoribbons.

$\boldsymbol{C}_h$	Ribbon width $[m]$	Edge	
		Ribbon	Tube
(n,n)	$2n$	Zigzag	Armchair
$(n,0)$	n	Armchair	Zigzag

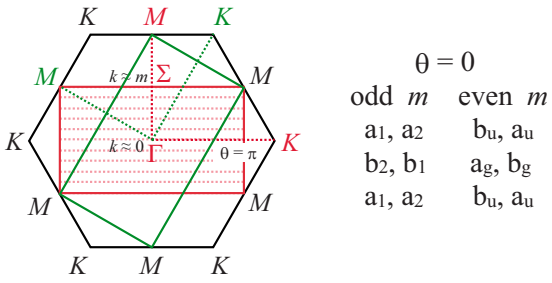

FIG. 2. (Color online) Brillouin zones for graphite (hexagon) and carbon nanoribbons (rectangle). High-symmetry points Γ, K, M, and Σ are defined for hexagonal lattices in conventional manners. θ is a phase difference between neighboring primitive units and k is the number of nodes in the width direction for $[m]$ zigzag nanoribbons. The symmetries of vibrations depend on the parity of k and m in an alternating manner at $\theta=0$.

The internal-coordinate force constants for nanoribbons were obtained from those of large PAHs comprising m honeycomb rows. The calculated force constants by the MO/8 model[38–42] were transformed into those in the Cartesian coordinates and zone folded for the primitive unit cells by weighting with the phase factor,

$$\boldsymbol{F} = \sum_{n=0}^{n_{\max}} F^{(n)} \cos n\theta, \tag{2}$$

where θ is the vibrational phase between neighboring units, $F^{(0)}$ is the force-constant matrix for the primitive unit cell, and $F^{(n\neq 0)}$ are the matrices describing interactions with the nth neighbor units. The interaction force constant matrices were found to be important for the convergence of acoustic modes to the zero frequency and several optical modes (details in Appendix E), although the magnitudes of $F^{(n\neq 0)}$ were not significantly large. For example, the root mean squares (rms's) of diagonal elements of $F^{(n\neq 0)}$ were calculated to be ~10% and ~1% of the unit-cell block $F^{(0)}$, respectively, at positions of $n=5$ and 10 in [20] zigzag ribbon. This fact is due to the group motion of delocalized π electrons. Thus, we set truncation thresholds for the interaction force constant matrices at $n_{\max}=11$ for zigzag ribbons and $n_{\max}=5$ for armchair ribbons. These thresholds were determined by increasing the size of PAHs from which force constants were obtained. The above thresholds required 21 rings in each row of PAHs. Thus, PAHs with 21 rings × 20 rows were calculated at maximum. The numerical errors due to the reduced symmetries of the finite-size PAHs were adjusted properly in accordance with the highest symmetries of the primitive units.

Figure 2 shows the Brillouin zones (BZs) for graphite and nanoribbons. The regular hexagon represented by the high-symmetry points of K and M corresponds to the BZ of graphite, where the ΓK distance is $4\pi/3a$ and $a=|\boldsymbol{a}_1|=|\boldsymbol{a}_2|$.[51,52] Accordingly, the translation vectors for zigzag and armchair ribbons are represented by the linear combinations of $\boldsymbol{a}_1-\boldsymbol{a}_2$ and $\boldsymbol{a}_1+\boldsymbol{a}_2$. Lengths are a and $\sqrt{3}a$, respectively, and corresponding reciprocal vectors are in the ΓK and ΓM directions. Therefore, BZ for zigzag and armchair ribbons are given by a rectangle of $3K/4\times M/2$ in Fig. 2, which is circumscribed by the original hexagonal BZ. The distance between zone center and edges is π/a for zigzag ribbons,[53] which is smaller by a factor of 3/4 than the ΓK distance. That for armchair ribbons is a half of the ΓM distance $\pi/(a\sqrt{3})$.

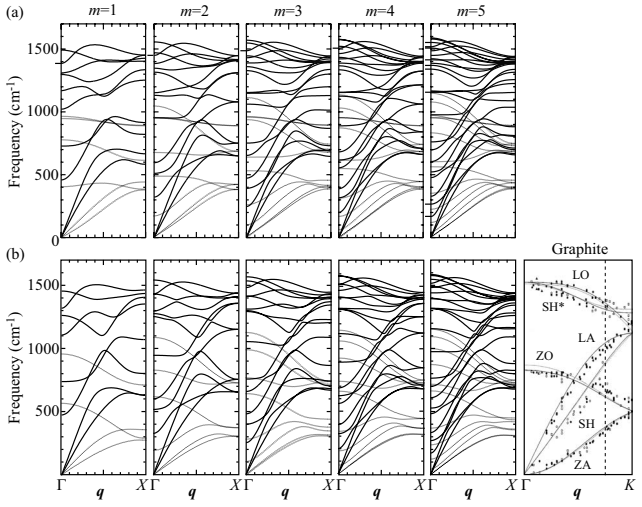

FIG. 3. Phonon dispersions of (a) hydrogenated and (b) dehydrogenated $[m]$ zigzag nanoribbons ($m=1-5$) in the Γ-K direction in comparison with those of graphite (Ref. 12). $X=3K/4$ and represents the boundary of the Brillouin zone at the wave vector unit π/a, i.e., phase difference π over lattice translation $|\mathbf{a}|$. Gray lines are out-of-plane modes.

III. RESULTS AND DISCUSSION

A. Dispersion curves of zigzag nanoribbons

Figure 3 presents phonon dispersion curves for zigzag nanoribbons in a range $m=1-5$ (a) with and (b) without hydrogen atoms as functions of $\boldsymbol{q}$ in comparison with those for graphite which were determined by electron energy loss spectroscopy.[12] Less-dispersive CH stretches are not shown here. The norm of primitive wave vector $\boldsymbol{q}$ is equal to the phase difference θ in Eq. (2) divided by the unit translation in the zigzag direction. The dispersion curves for $m=1$ in Fig. 3(a) are almost in good agreement with our previous results on polyacenes,[8] except for the highest longitudinal optical (LO) mode stemming from ~1400 cm^{-1} at the Γ point and the out-of-plane mode in a region of 400–500 cm^{-1}. The highest LO mode displays overbending (softening) toward the Γ point, which can be ascribed to the Kohn anomaly.[54] Interestingly, this overbending becomes smaller upon going to wider ribbons. The EPC over long distances are effectively involved in the force fields through bond-bond polarizability (Appendix C). Since the interaction matrices $F^{(n\neq 0)}$ included for zone folding in Eq. (2) were increased from $n_{\max}=5$ in the previous[8] work to $n_{\max}=11$ in the present work, long-range forces are described more properly. The inclusion of long-range interaction matrices will also create individual sample points near the Γ point. For complete treatments of long-range interactions, calculations

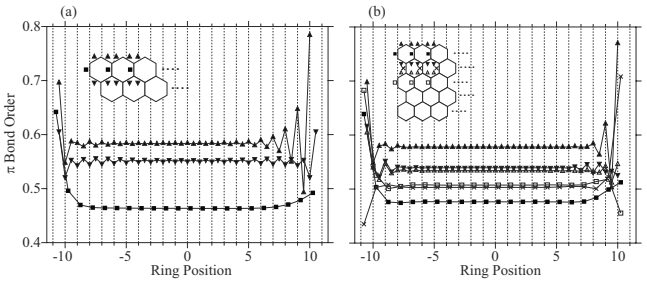

FIG. 4. Bond orders calculated for π electrons in PAHs with (a) 2 rows $\times$ 21 rings and (b) 5 rows $\times$ 21 rings, respectively.

based on Bloch wave functions would be required. The discrepancies found for the out-of-plane mode, which are $\sim$50 cm^{-1} at maximum, are likely to be due to the lack of long-range interaction force constants through the bond-bond polarizability in the present study.

In analogy with carbon nanotubes,[49,50] discrepancies are anticipated in the force fields of metallic and semiconducting phases. Since the electric conductivity in one-dimensional systems is affected by the Peierls instability, the most straightforward structural indication of the semiconducting phase would be the alternations of bond distances. Figure 4 shows the calculated bond orders for (a) two-row and (b) five-row PAHs. No significant bond alternations along the ribbons imply that the dominant force constants are close to those in the metallic phase. Similar bond characters have been obtained by DFT calculations for acene molecules up to 15 rings.[8] The bond alternations in the C_{2h} symmetry have not been obtained either by the Hückel and DFT calculations. Nonetheless, there remain subtleties as to whether the complete delocalization of π electron is possible in nanoribbons since the networks of zigzag nanoribbons consist of *trans*-polyacetylene chains, which display bond alternations in neutral states. Spin states are also yet to be investigated for the nanoscale structures between molecules and bulk materials.

B. Normal modes of carbon nanoribbons

The phonon dispersions of zigzag and armchair nanoribbons are reduced into the rectangular BZ, shown in Fig. 2, and one-dimensional dispersion relations are obtained in repeating directions. The symmetry of vibrations and optical selection rules at the Γ point (Appendix A) are dependent on the parity of the repeating unit shown in Fig. 1(b). All the normal modes are classified into (1) acoustic modes, (2) acoustic harmonics, (3) optical harmonics, and (4) CH modes. In the following, we discuss their vibrational patterns in connection with their commensurateness with ring structures.

1. Acoustic modes

The longitudinal (LA) and transverse acoustic (TA) modes converge to the origin as in Fig. 3. The sound velocities of the in-plane LA and TA modes in [5] zigzag ribbons are calculated to be 24 and 20 km/s, respectively, for wavelengths much longer than lattice units. These values are comparable with those of graphite surfaces (24 and 14 km/s),[10,54] in which the TA mode is calculated to be slower. The small reduced mass of motion in ribbon widths and/or the high bond orders of diagonal CC bonds (Fig. 4) are likely to be responsible for this discrepancy.

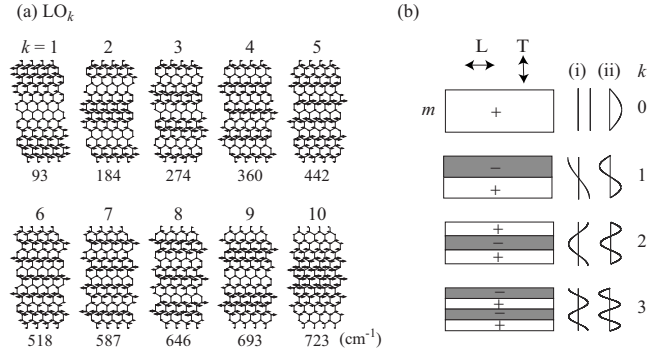

FIG. 5. (a) Longitudinal acoustic harmonics LO$_k$ (k=1, 2, . . . , m) for [10] zigzag nanoribbons at the Γ point and (b) a schematic showing the nodal structures in the direction of width. The nodes in amplitudes correspond to the characteristic vibrations of an elastic sheet with both ends (i) free or (ii) fixed.

The number of acoustic modes in nanoribbons is four due to the fact that rotations perpendicular to the one-dimensional lattice cannot be represented at the Γ point. The in-plane LA and TA modes are relevant to the LA and SH (shearing) mode of graphite, respectively. The two out-of-plane acoustic modes converge together onto the ZA (out-of-plane acoustic in z direction) mode of graphite upon going to larger m, as depicted by gray lines in Fig. 3. These out-of-plane acoustic modes possess rotational or translational characters at the Γ point, respectively. The corresponding acoustic modes in dehydrogenated ribbons are calculated to be $\sim$100 cm^{-1} lower.

2. Acoustic harmonics

All dispersion curves other than the four acoustic modes are optical branches. The finite width of nanoribbons imposes the boundary condition, which gives rise to vibrational harmonics in the width direction. Figure 5(a) shows a series of calculated harmonics for [10] zigzag nanoribbons. The patterns of vibrational amplitudes display significant relevance to those of elastic sheets illustrated in Fig. 5(b), with (i) free ends or (ii) fixed ends. The locations of the nodes are calculated to be independent of ring structures. The atomic displacements for all of the in-plane modes of zigzag nanoribbons were found to have pure T or L characters at the Γ point. In this paper, these optical modes are called *acoustic harmonics* or *elastic harmonics* with formal designations LO$_k$ and TO$_k$, where k is the number of nodes (k=1, 2, . . . , m). Their vibrational patterns are intrinsically correlated to the acoustic modes in the ΓM dispersion since k is in proportion to the wave number. Their frequencies do not converge to the origin at Γ, as can be seen as k series below 500 cm^{-1} for m=5 in Fig. 3. The acoustic fundamental modes of LA and TA literally correspond to LO$_0$ and TO$_0$, respectively.

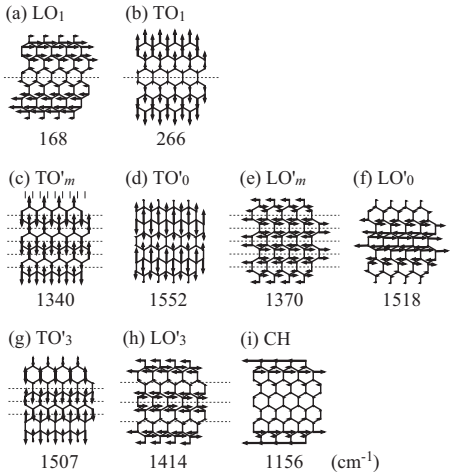

FIG. 6. Normal coordinates calculated for the optical modes of [5] zigzag nanoribbons at the Γ point. [(a) and (b)] elastic harmonics of LO_k and TO_k ($k=1,2,\ldots,m$), respectively. [(c)–(f)] optical modes that are commensurate with ring structures. [(g) and (h)] incommensurate optical harmonics. (i) CH bending mode.

3. Optical harmonics

Figure 6 presents the calculated in-plane modes for [5] zigzag ribbons at the Γ point, of which frequencies are depicted as outward lines on the left side of Fig. 3(a) for $m=5$. The vibrational displacements are calculated to be in either T or L directions at the Γ point. The optical modes without acoustic properties are called *optical harmonics* in this paper using primed symbols TO′ and LO′. The optical harmonics display the nodes of displacements within the primitive unit cells as the vertical lines depicted for TO'_m in Fig. 6(c), in contrast to the acoustic harmonics shown in Figs. 6(a) and 6(b). These antiphase displacements within units make it difficult to identify the phase relation of k.

When the positions of nodes are commensurate with ring structures in the width direction, the vibrational patterns are described by Wilson's notations for benzene rings.[55–57] The optical harmonics with $k=0$ and m shown in Figs. 6(c)–6(f) are commensurate with rings and correlations are found to be TO'_m: $19a$, TO'_0: $8a$, LO'_m: $19b$, and LO'_0: $8b$, where $19a/19b$ and $8a/8b$ are degenerate, respectively. The $k=0$ phase leads to additive effects in induced dipoles or polarizabilities for all rings in the unit and gives rise to significant optical activities at the Γ point. Indeed, the strong $G^{\pm}$ modes of bulk or nanoscale carbons are ascribed to the TO'_0 or LO'_0 modes. On the other hand, the incommensurate optical harmonics, TO'_k and LO'_k, where $k=1,2,\ldots,m-1$, are almost independent of the ring structures although the positions of nodes are restricted by CC bonds. For example, the vibrational patterns calculated for the $k=3$ modes of TO'_3 and LO'_3, shown in Figs. 6(g) and 6(h), display different positions of nodes and mode mixing between $19a+8a$ and $19b+8b$, respectively. These optical harmonics LO'_k and TO'_k are correlated to the LO and SH^* modes of graphite.[12]

It is noted that the parity of m (or $2m$ for armchair ribbons) gives rise to finite-width effects. In accordance with the positions of k nodal planes, the vibrational amplitudes of atomic displacements are located at vertical CC bonds and/or horizontal CCC junctions within the units. Hence, the existence or absence of the central hexagonal-ring rows, which depends on the parity of m, will determine the symmetries of vibrations. The horizontal positions of hexagonal-ring rows at both edges are also parity dependent. The edges of odd-m zigzag ribbons occupy identical positions in the horizontal direction in Fig. 1(b), whereas those of even-m zigzag ribbons are staggered half a ring. These different edge symmetries affect the localization of vibrations at edges and the inversion degeneracy of vibrations. The vibrational amplitudes at ribbon edges shown in Fig. 5(b) are governed by the commensurateness with ring structures. If opposite directions of displacements are constrained by nodal relations and symmetries at edges the amplitude is forced to be zero, as shown in Fig. 6(f).

The horizontal lines in Fig. 2 ($k\approx 0,\ldots,m$) illustrate the phonon dispersions in the ΓK direction for the $m+1$ discrete harmonics over the range of ΓΣ.[20,22] Another definition of the primitive unit cell is also possible with the orientation of the lattice fixed, such as that corresponding to the inclined rectangle. In this case, all of the $m+1$ lines are partitioned differently. The optical harmonics at the upper left M point display special vibrational patterns since this point are located at high-symmetry points for both horizontal and inclined BZ zones.

The out-of-plane optical harmonics are also obtained as k series in frequency regions lower than 600 and ~1000 cm^{-1}, respectively (see $m=4$ and 5 in Fig. 3). The lower-frequency series is assigned to acoustic harmonic series, and the higher-frequency one is the optical harmonics, which is a boat-type deformation correlated to the ZO (out-of-plane optical in z direction) mode of graphite. In general, the vibrational patterns of out-of-plane modes are calculated to appear simpler than the in-plane modes. The optical harmonics of hydrogenated and dehydrogenated zigzag ribbons are found to be similar [Figs. 3(a) and 3(b)].

4. CH modes

In-plane and out-of-plane CH bends are calculated to have small dispersions in regions of 1100–1200 and 900–1000 cm^{-1}, respectively. The two in-plane CH bends appear like additional lines with small dispersions for larger m in Fig. 3(a), whereas these CH bends are absent in Fig. 3(b). The fact that strong coupling between in-plane CH bends and CC vibrations was obtained for smaller m is ascribed to the large H/C ratios in the zigzag ribbons with $m=1-3$. The out-of-plane CH bends are calculated to remain relatively unchanged. Their flatness at 900–1000 cm^{-1} in Fig. 3(a) is due to the independence of neighboring CH bonds in the out-of-plane direction.

C. Width dependences of acoustic and optical harmonics

Figure 7 plots the Γ point frequencies for the k series of in-plane harmonics as a function of m for hydrogenated zigzag nanoribbons. The number of in-plane normal modes is $4m+8$ (given in Appendix A), all of the in-plane modes are presented except for CH stretches. The closed symbols de-

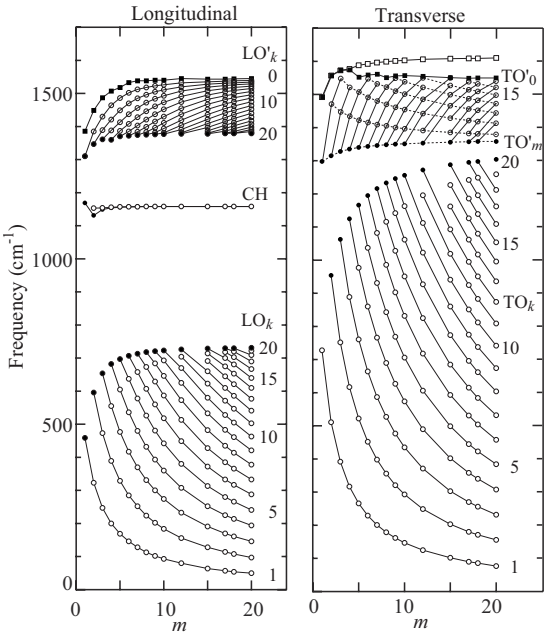

FIG. 7. Frequency shifts for the transverse and longitudinal modes of hydrogenated $[m]$ zigzag nanoribbons as a function of ribbon width (m) and the number of nodes $(k=1-m)$ in the direction of widths. Modes with the same k are connected with solid lines, and those of subtractive series $(k=m,m-1,\ldots)$ are connected by broken lines (see also Fig. 6).

note the vibrational phases with maximum (m) or minimum (0) k values, which are commensurate with ring structures. The incommensurate modes are depicted by open symbols. The frequencies of these k harmonics shift systematically in spite of their incommensurateness. The acoustic harmonics (unprimed) display greater frequency shifts than those of optical harmonics (primed). The global motion of the acoustic modes is likely to be responsible for this result. In general, the magnitudes of shifts are larger in transverse modes than in the longitudinal modes. Thus, the transverse G modes associated with $19a$ and $8a$ modes [Figs. 6(c) and 6(d), respectively] display wider dispersions. The very small frequency shifts calculated for the CH bends at ~ 1100 cm^{-1} suggest their independence.

The wave number in the ribbon width is proportional to k/m by definition, and frequencies at $(k,m)=(5,10)$, for instance, should be similar to those at (10,20). Deviations from this wave number relation indicate finite-size effects in widths or specificities at edges. It is of interest that not only acoustic harmonics but also the optical harmonics display the systematic frequency shifts. The LO$'_k$ and TO$'_k$ series in a region of 1400–1600 cm^{-1} stem from mixing between the $19b+8b$ and $19a+8a$ modes, respectively (Sec. III B 3). It is noted that TO$'_k$ gives rise to complicated series at ~ 1600 cm^{-1} for $m \geqslant 5$ in Fig. 7. The fact that the $k=0$ ends in the TO$'_k$ series (closed squares) are calculated lower than the $k \neq 0$ harmonics (open squares) is likely connected with the revival overbending in the ΓM direction for the LO mode of graphite.[11] Namely, the $k \neq 0$ modes with higher frequencies than the $k=0$ modes are overlapped twice in the wave vector region above the $k=0$ modes. The subtractive series in

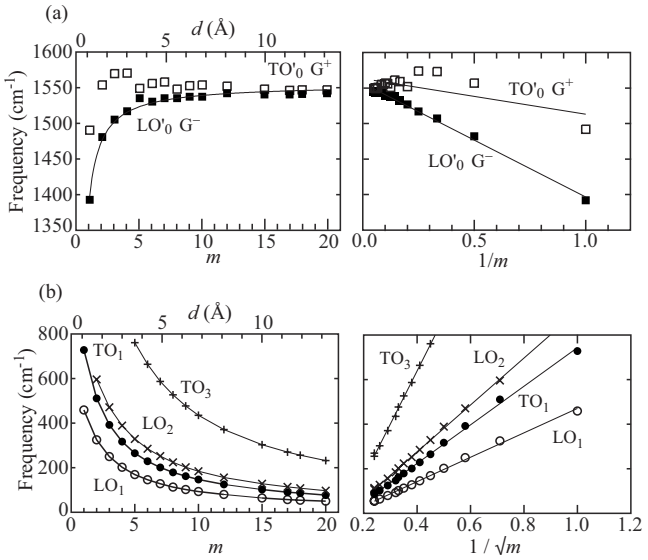

FIG. 8. Dependences for the vibrational frequencies of hydrogenated $[m]$ zigzag nanoribbons upon ribbon width m. (a) G^+ and G^- modes and (b) transverse and longitudinal acoustic harmonics with k nodes in the direction of widths TO$_k$ and LO$_k$ $(k=1-3)$.

terms of the number of rings, $k=m,m-1,m-2,\ldots$, are also indicated by broken lines in Fig. 7(b).

Figure 8 presents m dependencies for the acoustic and optical harmonics of $[m]$ zigzag nanoribbons. The frequencies of the LO$_k$ and TO$_k$ acoustic harmonics are proportional to $1/\sqrt{m}$, whereas those of the LO$'_0$ and TO$'_0$ optical harmonics to $1/m$, suggesting that different mechanics are involved. In particular, the $1/\sqrt{m}$ dependence for the acoustic harmonics is likely to be due to the properties of elastic continua. The deviations found for the TO$'_0$ modes may be related to the frequency inversions mentioned above. Table II presents the parameters fitted by regression analyses. The LO$_k$ and TO$_k$ acoustic harmonics with larger k numbers display greater dependences upon ribbon widths m.

As listed in Table I, the number of honeycomb rows in $[m]$ dehydrogenated zigzag nanoribbons is equal to that in $(m/2,m/2)$ armchair nanotubes. The nominal diameter calculated by $d=\sqrt{3}\times am/(2\pi)$ (Refs. 51 and 52) is presented as the upper scales in Fig. 8. The TO$'_0$-LO$'_0$ splitting correspond to the G band splitting in the Raman spectra of carbon nanotubes.[49] It is known that empirical fits by the first- or second-order regression forms like $\Delta\tilde{\nu}_G=-C/d^n$ $(n=1,2)$ give different series for metallic and semiconductor nanotubes.[22,50] The first-order dependence for the splitting is calculated to be $C=165$ cm^{-1} Å for the nanoribbons in a range $d=0.7-13$ Å. This dependence is much smaller than that for metallic nanotubes, $C=637$ cm^{-1} Å,[22,50] and almost negligible in zigzag ribbons with $m \geqslant 10$. Since the TO$'$ and LO$'$ modes are degenerated in the regular hexagonal lattice, the calculated splitting is ascribed to the anisotropy for ribbon widths $m<10$.

D. Dispersion curves of armchair nanoribbons

Figure 9 shows the dispersion curves of (a) hydrogenated and (b) dehydrogenated nanoribbons of armchair types, re-

TABLE II. Parameters fitted to the frequencies of elastic and optical harmonics of zigzag nanoribbons.

	LO_k: $\nu=a+b/\sqrt{m}$		TO_k: $\nu=a+b/\sqrt{m}$	
k	a (cm^{-1})	b (cm^{-1})	a (cm^{-1})	b (cm^{-1})
1	−76	547	−121	866
2	−148	1065	−242	1709
3	−194	1493	−320	2408
4	−226	1861	−379	3028
5	−247	2177	−424	3579
6	−256	2437	−460	4084
7	−259	2657	−484	4533
8	−250	2824	−500	4935
9	−234	2953	−507	5290
10	−243	3171	−522	5663
11	−177	3069	−506	5899
12	−225	3432	−534	6303
13	−156	3290	−499	6435
14	−55	2993	−456	6519
15	−74	3195	−482	6878
	LO_0': $\nu=a'+b'/m$		TO_0': $\nu=a'+b'/m$	
k	a' (cm^{-1})	b' (cm^{-1})	a' (cm^{-1})	b' (cm^{-1})
0	1557	−160	1563	−50

spectively, in comparison with those of graphite.[11] The ΓM dispersions of graphite are folded into the half Brillouin zone of $\Gamma\Sigma$, as shown in Fig. 2. The hydrogen atoms give rise to the dispersion curves of in-plane and out-of-plane CH bends at 1150 and 950 cm^{-1}, respectively, and do not cause significant changes. The small magnitudes of frequency shifts are due to the small distance of $\Gamma\Sigma$ or the long unit distances in real space, which emphasize the independence of ring structures. Folding back the dispersion curves of graphite at Σ makes positive slopes to negative ones. Correspondingly, the ZA, SH, and LA modes of graphite show negative slopes and the ZO, SH^*, and LO modes positive ones. These inversions are remarkably reproduced in the dispersion curves of nanoribbons.

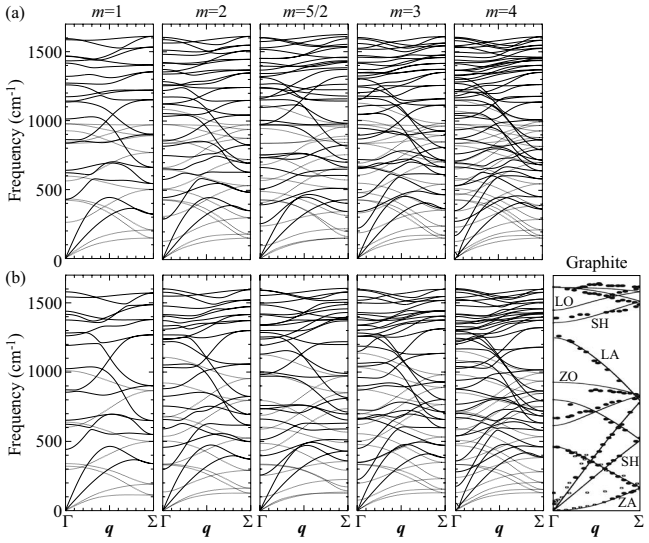

FIG. 9. Phonon dispersions of (a) hydrogenated and (b) dehydrogenated $[m]$ armchair nanoribbons ($m=1-4$) in the Γ-M (Σ) direction in comparison with those of graphite (Ref. 11). Σ represents the boundary of the Brillouin zone, i.e., at Σ phase difference is π over lattice translation $|\boldsymbol{a}_1-\boldsymbol{a}_2|$. Gray lines correspond to out-of-plane modes.

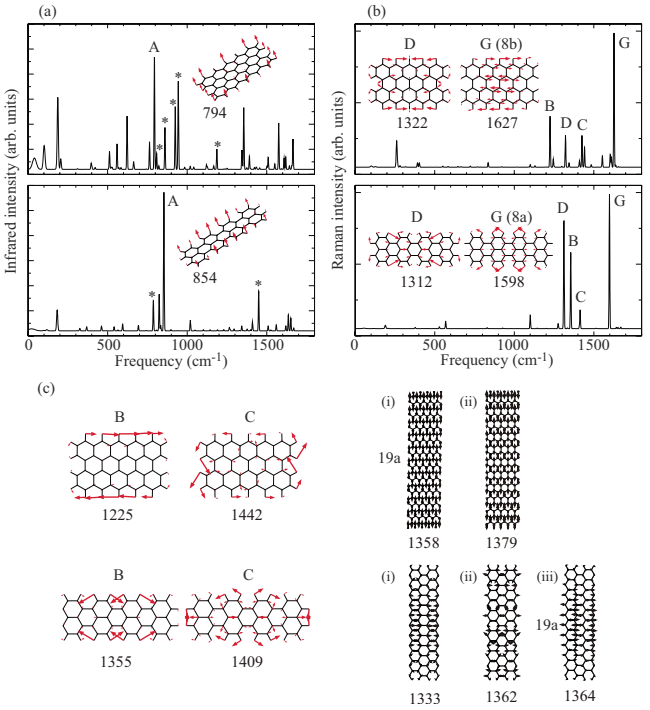

FIG. 10. (Color online) (a) Infrared and (b) nonresonant Raman spectra calculated for polycyclic aromatic hydrocarbons of zigzag and armchair types at the B3LYP/4-31G level of theory. The bands have been convoluted with Gaussian bandwidths that are proportional to the thermal factor at 300 K. Asterisks denote CH bending modes. (c) Vibrational mode patterns calculated for zigzag and armchair PAHs, [20] zigzag and [10] armchair nanoribbons.

E. Infrared and Raman activity

Figure 10 presents the infrared and nonresonant Raman spectra calculated for finite-size PAHs with zigzag and armchair edges at the B3LYP/4-31G(d) level of density functional theory using the GAUSSIAN 03 program.[58] The strongest infrared bands are assigned to out-of-plane CH bends shown in Fig. 10(a), which are commonly observed for PAHs.[35,36] The calculated Raman spectra are in line with the previous study at the BLYP/6-31G level by Negri *et al.*[59] Since the longitudinal and transverse directions are interchanged between zigzag and armchair ribbons, we use notations 8a and 8b (Refs. 55–57) which are correlated with TO_0' and LO_0' in zigzag ribbons, respectively, and LO_0' and TO_0' in armchair ribbons. Modes 8b and 8a give rise to the strongest G bands for the zigzag and armchair PAHs, respectively, in Fig. 10(b). Both of the G modes are correlated to the LO_0' modes in

TABLE III. Observable vibrational frequencies (cm^{-1}) in carbon nanoribbons and nanotubes, graphite, and PAHs comprising 7–50 rings.

	Calc.		Expt.								
					PAH[b]						
Mode	Zigzag (10,10)[c]	Armchair (10,0)[c]	CNT[a] (15,2)	Graphite	7[d]	13	20	24	27	34	50
G	1550 1545	1565 1544	1590 1560	1575,1581[e]	1627	1604	1601	1603	1597	1603	1597
D	1379[f] 1358[g]	1364[g] 1333[f]		1355[h]	1349	1304 1262	1334 1260	1339 1253	1333 1261	1316 1253	1310 1236
Out of plane				868[i]							

[a]Raman bands at 488.0 nm excitation. Taken from Ref. 50.
[b]Reference 7.
[c]The (10,10) and (10,0) chiral vectors correspond to [20] zigzag and [10] armchair nanoribbons, respectively.
[d]The number of rings.
[e]Raman bands of highly oriented pyrolytic graphite taken from Refs. 62 and 61, respectively. This mode shows frequency shifts and becomes infrared active upon grinding (Ref. 60).
[f]Superlattices are not assumed. Vertical CC stretches [see Fig. 10(c)].
[g]Superlattices are not assumed. Close to mode 19*a*.
[h]Reference 62.
[i]Reference 61.

zigzag and armchair nanoribbons. Table III compares the calculated Raman bands for zigzag and armchair nanoribbons with the experimentally determined Raman bands for graphite,[60,61] carbon nanotubes (CNTs),[50] and PAHs.[7] The splitting of *G* mode is calculated to be slightly larger in [10] armchair ribbon than in [20] zigzag ribbon.

It is widely accepted that the origin of the *D* bands at $\sim$1350 cm^{-1} is due to totally symmetric modes with breathing characters which are activated by superlattices originating from defects or boundary edges.[7,62,63] The totally symmetric modes obtained as modes *B*, *C*, and *D* in Fig. 10 indeed give rise to strong Raman bands for finite-size PAHs.[59] However, the breathinglike modes are obtained only at zone edges for zigzag and armchair nanoribbons. The potential candidates for the *D* modes were chosen from the Γ-point modes of nanoribbons in the range of 1300–1400 cm^{-1} in Table III and Fig. 10(c). The vibrational patterns of these optical modes (i)–(iii) are significantly different from those of finite-size PAHs in that optical displacements in the units are exactly repeated. Moreover, all of modes (i)–(ii) in zigzag ribbons display opposite displacements within the repeating units at equivalent CC bonds or CCC angles, and modes (i)–(iii) in armchair ribbons also show opposite displacements between vertical honeycomb rows. Hence, resultant cancellation effects by the balanced displacements would lead to weak nonresonant Raman intensities from carbon networks in nanoribbons.

In-plane CH bends can couple with ring vibrations as calculated for modes *B* and *D* in the finite PAHs in Fig. 10 and several larger PAHs with armchair edges.[59] However, the strong Raman activities are due to vibrations of carbon moieties in these cases, and significant changes of molecular volumes are also involved. Conversely, in the case of nanoribbons, the additional dispersion curves from in-plane CH bends are relatively unchanged at $\sim$1150 cm^{-1}, particularly in wider ribbons [Figs. 3(a) and 9(a)]. The changes of volumes are not expected due to the $\theta=0$ condition at the Γ point. Therefore, nonresonant Raman intensities could be activated in a region $\sim$1350 cm^{-1} only by displacements localized at finite lengths or edges.

The resonance Raman effects have been observed and calculated for the bond-alternating vibrations of Kekulé type (similar to mode *D* in Fig. 10), totally symmetric CH bends, and mode 8*b* (similar to mode *G* in Fig. 10) for linear PAHs of zigzag types.[8] The Kekulé-type vibrations (mode 14 of benzene)[55–57] are also obtained as mode (ii) of armchair ribbons. These facts indicate that CH bending modes and Kekulé vibrations could give rise to strong Raman intensities through the resonance Raman effects. In particular, the Γ-point modes in armchair ribbons are not separated into longitudinal and transverse modes, and therefore can Kekulé vibrations can appear at the Γ point.

F. Edge-localized vibrations

The boundary conditions imposed by finite ribbon widths lead to special edge-localized states, such as those electronic states localized at zigzag edges.[17,18] In this work, localization of vibrations was calculated to take place only in armchair ribbons. The edge-localized modes are obtained in hydrogenated and dehydrogenated analogs at $\sim$680–700 cm^{-1} over one or two rings from edges, whereas inner-localized modes are also calculated as modes (i) and (iii) in Fig. 10(c). The edge structures have been well studied for PAHs in connection with the periphery shapes of ring structures.[27,64] In particular, the out-of-plane CH bends is known to be a marker of the perimeters of PAHs in infrared spectra. The CH bonds are categorized according to the number of adjacent CH bonds. A general tendency of frequencies is solo (nonadjacent CH bonds): $\sim$900 cm^{-1}, duo (doubly adjacent CH

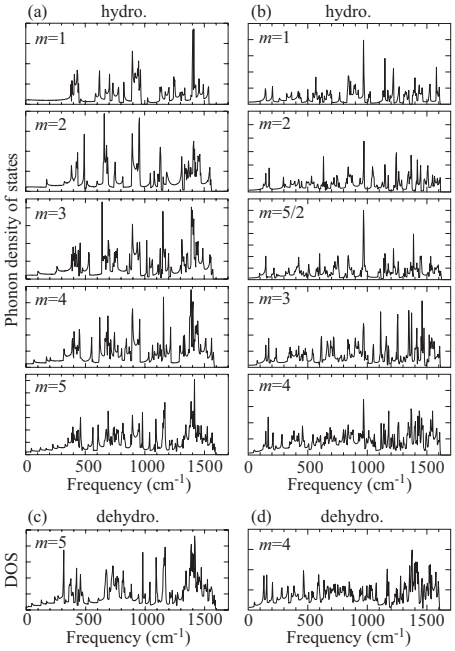

FIG. 11. Phonon densities of states for [m] hydrogenated nanoribbons ($m=1-5$) of (a) zigzag and (b) armchair types, and those for dehydrogenated nanoribbons of (c) zigzag and (d) armchair types, respectively.

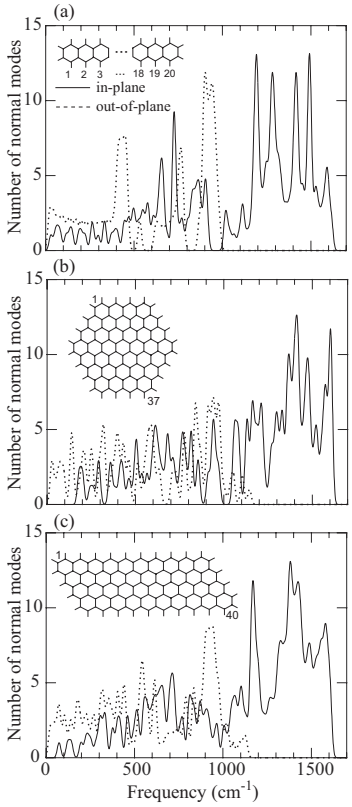

FIG. 12. Distributions of normal modes for polycyclic aromatic hydrocarbons with (a) linear, (b) round, and (c) rectangular shapes. A full width at half maxima Gaussian bandwidth of 10 cm^{-1} with a unit height has been convoluted to each vibrational state.

bonds): 800–850 cm^{-1}, trio (three CH groups): ~760 cm^{-1}, and quartet (four CH bonds): 740 cm^{-1}.[64] The out-of-plane CH bends in nanoribbons are calculated to match this tendency, solo CH groups in zigzag ribbons and duo CH groups in armchair ribbons appear at 950 and 840 cm^{-1}, respectively [Figs. 3(a) and 8(a)]. Therefore, the hydrogenated edges of zigzag or armchair types can be determined in principle by the localized Raman modes of Kekulé type or the infrared-active out-of-plane CH bends.

G. Density of states

Figure 11 shows the density of states (DOS) for zigzag and armchair nanoribbons with edges hydrogenated and dehydrogenated, respectively. The bunches of peaks are obtained almost selectively for zigzag ribbons at ~1400 and ~400 cm^{-1}. Contributions from CH bonds are distinguished by comparing the hydrogenated and dehydrogenated ribbons. The out-of-plane CH bends give rise to peaks at 850–950 cm^{-1} for the solo CH bonds in hydrogenated zigzag ribbons and a sharp peak at 980 cm^{-1} for the duo CH bonds in armchair ribbons, whereas the in-plane CH bends are overlapped by other peaks. It should be recalled that peaks in DOS represent the averaged frequencies over $\boldsymbol{q}$.

Figure 12 presents the DOS of in-plane and out-of-plane modes for three types of PAHs with linear, round, and rectangular periphery. The linear PAH displays peaks at ~400 and ~900 cm^{-1}, which are assigned to boat deformations and out-of-plane CH bends, respectively. The round PAH does not show similar peaks, whereas the rectangular one displays marginally. It follows that the two DOS peaks are unique for linear PAHs. Similar DOS peaks are obtained for hydrogenated zigzag ribbons only [Fig. 11(a)]. Hence, the origins of these peaks are likely to be connected with the translational symmetry of zigzag type.

IV. CONCLUSIONS

In the phonon dispersion curves of carbon nanoribbons of zigzag and armchair types, all normal modes give rise to acoustic or optical harmonics in systematic propensities. The MO/8 force fields, which are applicable to arbitrary PAHs larger than 400 rings, can be transferred to repeating structures by the zone-folding method. The molecular-spectroscopic approach presented in this paper can bridge molecular vibrations and phonons of solids, in which periodic and local structures can be investigated. The fact that experimental data for different kinds of PAHs are reproduced (Ref. 42, Appendixes C and D) is promising since any kind of nanoscale carbons can be studied. In particular, high-performance computers can allow us to calculate more sophisticated properties of nanoscale carbons, such as the resonance Raman effect[8] and vibronic coupling at the excited states.[42]

ACKNOWLEDGMENTS

This work was supported by 21st century COE program from the ministry of Education, Science, Sports, and Culture

TABLE IV. Symmetry of vibrations for the primitive unit cells in $[m]$ carbon nanoribbons.

(n,n) zigzag ribbon					$(n,0)$ armchair ribbon				
m[a]	Sym.		Infrared	Raman	m[a]	Sym.		Infrared	Raman
Odd	C_{2v}	$\Gamma^{ip}=(2m+4)a_1$	a	a	Half integer	D_{2h}	$\Gamma^{ip}=(2m+4)a_g$		a
		$(2m+4)b_2$	a	a			$(2m+4)b_{3g}$		a
		$\Gamma^{op}=(m+2)b_1$	a	a			$(2m+4)b_{1u}$	a	
		$(m+2)a_2$		a			$(2m+4)b_{2u}$	a	
							$\Gamma^{op}=(m+5/2)b_{1g}$		a
							$(m+3/2)b_{2g}$		a
							$(m+3/2)a_u$		
							$(m+5/2)b_{3u}$	a	
Even	C_{2h}	$\Gamma^{ip}=(2m+4)a_g$		a	Integer	C_{2v}	$\Gamma^{ip}=(4m+8)a_1$	a	a
		$(2m+4)b_u$	a				$(4m+8)b_2$	a	a
		$\Gamma^{op}=(m+2)b_g$		a			$\Gamma^{op}=(2m+4)b_1$	a	a
		$(m+2)a_u$	a				$(2m+4)a_2$		a

[a]m is defined by the number of rows [see Fig. 1(b) and Table I].

of Japan, by a Grant-in-Aid for Scientific Research (C) from the Japan Society for the Promotion of Science, and partially by a grant from the Matsuo Foundation. The authors thank S. Siebentritt for her permission to include Fig. 4 of Ref. 12 and C. Oshima for his permission to reproduce Fig. 6 of Ref. 11.

APPENDIX A: IRREDUCIBLE REPRESENTATIONS

Table IV presents symmetry properties and vibrational selection rules for zigzag and armchair hydrogenated ribbons, which depend on the parity of m (zigzag) or $2m$ (armchair). The point groups for the primitive unit cells of zigzag ribbons are C_{2v} (even m) or C_{2h} (odd m), whereas those for armchair ribbons are D_{2h} (integer m) or C_{2v} (half-integer m), respectively. The selection rules for infrared and Raman transitions are derived from the irreducible representations at the Γ point, which can be decomposed into in-plane and out-of-plane vibrations. The existence of the inversion center in the unit cell results in the mutual exclusivity rule. These Γ-point symmetries are not valid when the wave vector of phonon $\boldsymbol{q}$ is nonzero. Instead, the factor group of total lattices will determine selection rules for $\boldsymbol{q}$-sensitive phenomena and crossing-anticrossing conditions for dispersion curves.

APPENDIX B: INTERNAL COORDINATES

Figure 13 illustrates the internal coordinates employed in this work. They were defined in a conventional manner[65] for stretching (R_i and r_j), bending ($\alpha_k-\alpha_k''$), out-of-plane displacement (θ_l), and torsional (t_m) vibrations. The advantages of the internal coordinates over the Cartesian-based coordinates are related to the nature of chemical bonding. Vibrational properties such as force constants are in general associated with chemical bonds and can be represented directly by the internal coordinates. The drawbacks were the arbitrariness of choosing internal coordinates and redundancy. In this work, redundant coordinates for angles $\alpha_k-\alpha_k''$ were eliminated by setting up two orthonormal linear combinations of $\Delta\alpha_k-\Delta\alpha_k''$ as local symmetry coordinates,[56] and those associated with rings were reduced by transforming the secular equation to a symmetric form by Miyazawa's method.[66]

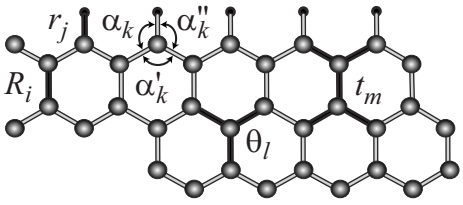

FIG. 13. In-plane and out-of-plane internal coordinates.

APPENDIX C: IN-PLANE MODES

In-plane vibrations involving stretches and bends were calculated based on the force-field model which we call the MO/8 model.[38–42] The predictivity of this model has been confirmed for a test set of PAHs comprising up to 12 rings (benzene, naphthalene, anthracene, naphthacene, pyrene, triphenylene, pentacene, perylene, benzo$[g,h,i]$perylene, coronene, ovalene, tribenzo$[a,g,m]$coronene, and kekuléne). The resultant rms frequency errors have been found to be only ~ 20 cm^{-1}, i.e., $\sim 3\%$.[42] The qualities of the calculated normal coordinates have also been found to be as reliable as DFT calculations.[67] Systematic tendencies for the nanoscale honeycomb networks could be gained with non-*ab initio* calculations. A short computational time allows us to perform calculations for sophisticated properties such as vibronic bands for electronically excited states[42] and resonance Raman effects.[8]

Details for the MO/8 model are given in Refs. 38–42. Briefly, the force constants for R_i are calculated based on the bond orders (BOs) and bond-bond polarizabilities (BBPs), which describe the long-range coupling of CC stretches through the motion of π electrons. The diagonal and off-diagonal force constants are obtained as

$$F_{ii}(\mathrm{CC}) = f_1 + f_2(P_i - P_0) + f_3(\Pi_{ii} - \Pi_0), \quad \text{(C1)}$$

$$F_{ij}(\mathrm{CC/CC}) = f_3\Pi_{ij} \quad (i \neq j), \quad \text{(C2)}$$

where P_i is BO for ith CC bond and Π_{ij} is BBP between ith and jth CC bonds, and P_0 and Π_0 are those for benzene as standard. Other force constants are set to be constant: $f_4 = F(\mathrm{CH})$, $f_5 = F(\mathrm{CCC})$, $f_6 = F(\mathrm{CCH})$, $f_7 = F(\mathrm{CC/CCC})$, and $f_8 = F(\mathrm{CC/CCC})$. These eight parameters are chosen as the averages of those optimized independently for five kinds of PAHs (benzene, naphthalene, anthracene, pyrene, and triphenylene), being $f_1 = 6.821$, $f_2 = 5.450$, $f_3 = 3.646$, $f_4 = 5.072$, $f_5 = 0.928$, $f_6 = 0.504$, $f_7 = 0.430$, and $f_8 = 0.199$ in the appropriate units either of 10^2 N m^{-1}, 10^{-18} N m rad^{-2}, 10^{-8} N rad^{-1}, or $10^2\beta$ N m^{-1}, respectively. P_i between atoms a and b and Π_{ij} are obtained from molecular orbital calculations of Hückel theory with resonance energy $\beta = -1$,

$$P_i = 2\sum_{k}^{\mathrm{occ}} C_{ka}C_{kb}, \quad \text{(C3)}$$

$$\Pi_{ij} = \partial P_i/\partial\beta_j, \quad \text{(C4)}$$

where C_{ka} are the kth MO coefficient for atom a, and the summation of k runs over the occupied orbitals. The MO coefficients were obtained from the secular determinants represented based on

Coulomb integral:

$$\alpha_a = \int \phi_a^* h \phi_a d\tau, \quad \text{(C5)}$$

resonance integral:

$$\beta_{ab} = \int \phi_a^* h \phi_b d\tau \quad (a \neq b), \quad \text{(C6)}$$

overlap integral:

$$S_{ab} = \int \phi_a^* \phi_b d\tau \quad \text{(C7)}$$

for π orbitals. All Coulomb integrals were set to be constant and normalized by resonance integrals between adjacent C atoms, which were set to be a parameter β. Overlap integrals were neglected. The perturbation theory treatments derived by Coulson and Longuet-Higgins[43–46] allow us to calculate Π_{ij} from (C_{ka}) in a short computational time. For example, the computation of force fields for a PAH with 380 rings takes ~20 h on a single Pentium®-based personal computer. This computational time could be significantly reduced by utilizing high-performance computes. The geometrical structures are assumed to be regular hexagons with CC distance of benzene, 1.397 Å, and capped by CH bonds of 1.084 Å.[68] The resultant lattice constant is $a = 2.420$ Å, which is slightly shorter than the experimental value for graphite, 2.478 Å (Ref. 69). Geometrical deviations from the above CC distance deviations are effectively involved in the diagonal CC force constant in Eq. (C1).

APPENDIX D: OUT-OF-PLANE VIBRATIONS

Out-of-plane vibrations were calculated by modifying the model reported by Cyvin *et al.*[70,71] The force constants were the same, but regular hexagons were assumed. The rms error between the calculated and experimental frequencies of PAHs (naphthalene, anthracene, coronene, and kekuléne) was calculated to be 24.2 cm^{-1}, whereas it was 22.5 cm^{-1} when the hexagons were distorted using the bond order.[70,71] In general, interaction force constants for carbons at distant positions play an important role in the delocalized π electrons, and geometrical structures can be regarded as circumstantial properties which are determined by such interactions.

APPENDIX E: LONG-RANGE INTERACTION

In the zone-folding procedures, long-range interactions were included through off-diagonal force constants, $F^{(n\neq 0)}$ in Eq. (2). Table V shows calculated frequencies when varying the length (n) of PAHs from which force constants were obtained and the truncation thresholds $(n_{\max})$ for the range of interactions. Beyond $n_{\max} \geqslant 6$ the frequencies become constant and acoustic modes converge to the zero frequency. Hence, we employed $n = 21$ and $n_{\max} = 11$ in this paper.

TABLE V. Calculated frequencies (cm^{-1}) for the in-plane modes of [2] zigzag ribbons at Γ point using force constants taken from a PAH with 2 rows × n rings. Interactions between up to the $n_{\max}$th neighbors are included.

n	7	9	11	13	15					21			
$n_{\max}$	4	5	6	7	4	5	6	7	8	5	6	10	11
mode 3	1561	1559	1558	1557	1556	1556	1556	1557	1557	1556	1556	1556	1556
mode 4	1506	1487	1474	1470	1474	1470	1470	1470	1470	1470	1470	1470	1470
mode 5	1475	1472	1471	1466	1470	1463	1463	1461	1460	1460	1456	1450	1449
mode 15	41	29	19	11	24	18	18	12	7	23	17	4	3
mode 16	16	11	8	6	21	9	9	6	5	14	10	3	3

[1] A. C. Ferrari, J. C. Meyer, V. Scardaci, M. Lazzeri, F. Mauri, S. Piscanec, D. Jiang, K. S. Novoselov, S. Roth, and A. K. Geim, Phys. Rev. Lett. **97**, 187401 (2006).
[2] G. M. Rutter, J. N. Crain, N. P. Guisinger, T. Li, P. N. First, and J. A. Stroscio, Science **317**, 219 (2007).
[3] C. Berger, Z. Song, X. Li, X. Wu, N. Brown, C. Naud, D. Mayou, T. Li, J. Hass, A. N. Marchenkov, E. H. Conrad, P. N. First, and W. A. de Heer, Science **312**, 1191 (2006).
[4] L. C. Venema, J. W. G. Wildöer, H. L. J. T. Tuinstra, C. Dekker, A. G. Rinzler, and R. E. Smalley, Appl. Phys. Lett. **71**, 2629 (1997).
[5] M. Furuhashi and T. Komeda, Jpn. J. Appl. Phys., Part 2 **46**, L161 (2007).
[6] T. Yumura, D. Nozaki, S. Bandow, K. Yoshizawa, and S. Iijima, J. Am. Chem. Soc. **127**, 11769 (2005).
[7] C. Castiglioni, C. Mapelli, F. Negri, and G. Zerbi, J. Chem. Phys. **114**, 963 (2001).
[8] Y. Yamakita, J. Kimura, and K. Ohno, J. Chem. Phys. **126**, 064904 (2007).
[9] R. Nicklow, N. Wakabayashi, and H. G. Smith, Phys. Rev. B **5**, 4951 (1972).
[10] C. Oshima, T. Aizawa, R. Souda, Y. Ishizawa, and Y. Sumiyoshi, Solid State Commun. **65**, 1601 (1988).
[11] T. Aizawa, R. Souda, S. Otani, and Y. Ishizawa, and C. Oshima, Phys. Rev. B **42**, 11469 (1990).
[12] S. Siebentritt, R. Pues, K.-H. Rieder, and A. M. Shikin, Phys. Rev. B **55**, 7927 (1997).
[13] J. Maultzsch, S. Reich, C. Thomsen, H. Requardt, and P. Ordejón, Phys. Rev. Lett. **92**, 075501 (2004).
[14] R. J. Nemanich, G. Lucovsky, and S. A. Solin, Mater. Sci. Eng. **31**, 157 (1977).
[15] A. Grüneis, R. Saito, T. Kimura, L. C. Concado, M. A. Pimienta, A. Jorio, A. G. Souza Filho, G. Dresselhaus, and M. S. Dresselhaus, Phys. Rev. B **65**, 155405 (2002).
[16] R. A. Jishi, Venkataraman, M. S. Dresselhaus, and G. Dresselhaus, Chem. Phys. Lett. **209**, 77 (1993).
[17] M. Fujita, K. Wakabayashi, K. Nakada, and K. Kusakabe, J. Phys. Soc. Jpn. **65**, 1920 (1996).
[18] K. Nakada, M. Fujita, G. Dresselhaus, and M. S. Dresselhaus, Phys. Rev. B **54**, 17954 (1996).
[19] Y. Miyamoto, M. L. Cohen, and S. G. Louie, Phys. Rev. B **52**, 14971 (1995).
[20] J. Yu, R. K. Kalia, and P. Vashishta, J. Chem. Phys. **103**, 6697 (1995).
[21] D. Sánchez-Portal, E. Artacho, J. M. Soler, A. Rubio, and P. Ordejón, Phys. Rev. B **59**, 12678 (1999).
[22] O. Dubay and G. Kresse, Phys. Rev. B **67**, 035401 (2003).
[23] L. Wirtz and A. Rubio, Solid State Commun. **131**, 141 (2004).
[24] E. Clar, *Polycyclic Hydrocarbons* (Academic, New York, 1964).
[25] J. B. Birks, *Photophysics of Aromatic Molecules* (Wiley, London, 1970).
[26] W. Karcher, R. J. Fordham, J. J. Dubois, P. G. J. M. Glaude, and J. A. M. Ligthart, *Spectral Atlas of Polycyclic Aromatic Compounds: Including Data on Occurrence and Biological Activity* (Kluwer, Hingham, MA, 1985), Vols. 1 and 2.
[27] Léger, A, L. d'Hendecourt, and N. Boccara, *Polycyclic Aromatic Hydrocarbons and Astrophysics*, NATO ASI Series (Reidel, Holland, 1987).
[28] R. G. Harvey, *Polycyclic Aromatic Hydrocarbons* (Wiley-VCH, New York, 1997).
[29] S. Krasnokutski, G. Rouillé, and F. Huisken, Chem. Phys. Lett. **406**, 386 (2005).
[30] H. Sellers, P. Pulay, and J. E. Boggs, J. Am. Chem. Soc. **107**, 6487 (1985).
[31] F. Negri and M. Zgierski, J. Chem. Phys. **104**, 3486 (1996).
[32] J. Szczepanski, M. Valla, D. Talbi, O. Parisel, and Y. Ellinger, J. Chem. Phys. **98**, 4494 (1993).
[33] S. Zilberg, Y. Haas, and S. Shaik, J. Phys. Chem. **99**, 16558 (1995).
[34] D. Chakaraborty, R. Ambashta, and S. Manogaran, J. Phys. Chem. **100**, 13963 (1996).
[35] S. R. Langhoff, J. Phys. Chem. **100**, 2819 (1996).
[36] D. M. Hudgins and S. A. Sandford, J. Phys. Chem. A **102**, 329 (1998).
[37] T. Tanaka, A. Tajima, R. Moriizumi, M. Hosoda, R. Ohno, E. Rokuta, C. Oshima, and S. Otani, Solid State Commun. **123**, 33 (2002).
[38] K. Ohno, J. Mol. Spectrosc. **72**, 238 (1978).
[39] K. Ohno, Chem. Phys. Lett. **70**, 536 (1980).
[40] K. Ohno, J. Chem. Phys. **95**, 5524 (1991).
[41] K. Ohno and H. Shinohara, J. Phys. Chem. **98**, 10063 (1994).
[42] K. Ohno, R. Takahashi, M. Yamada, and Y. Isogai, Internet Electron. J. Mol. Des. **636**, 1 (2002).
[43] C. A. Coulson and H. C. Longuet-Higgins, Proc. R. Soc. London, Ser. A **191**, 39 (1947).
[44] C. A. Coulson and H. C. Longuet-Higgins, Proc. R. Soc. London, Ser. A **192**, 16 (1947).
[45] C. A. Coulson and H. C. Longuet-Higgins, Proc. R. Soc. London, Ser. A **193**, 447 (1948).
[46] C. A. Coulson and H. C. Longuet-Higgins, Proc. R. Soc. London, Ser. A **193**, 456 (1948).
[47] T. Kakitani, Prog. Theor. Phys. **51**, 656 (1974).
[48] C. Mapelli, C. Castiglioni, and G. Zerbi, Phys. Rev. B **60**, 12710 (1999).
[49] E. D. Donato, M. Tommasini, C. Castiglioni, and G. Zerbi, Phys. Rev. B **74**, 184306 (2006).
[50] A. Jorio, A. G. Souza Filho, G. Dresselhaus, M. S. Dresselhaus, A. K. Swan, M. S. Ünlü, B. B. Goldberg, M. A. Pimenta, J. H. Hafner, C. M. Lieber, and R. Saito, Phys. Rev. B **65**, 155412 (2002).
[51] M. S. Dresselhaus, G. Dresselhaus, and R. Saito, Carbon **33**, 883 (1995).
[52] R. Saito, G. Dresselhaus, and M. S. Dresselhaus, *Physical Properties of Carbon Nanotubes* (Imperial College Press, London, 1998).
[53] The definition of primitive unit vectors of $\boldsymbol{a}_1=(\sqrt{3}/2,1/2)a$ and $\boldsymbol{a}_2=(\sqrt{3}/2,-1/2)a$ gives the reciprocal vectors $\boldsymbol{b}_1=(1/\sqrt{3},1)2\pi/a$ and $\boldsymbol{b}_2=(1/\sqrt{3},-1)2\pi/a$. The linear combinations of $\boldsymbol{a}_1-\boldsymbol{a}_2=(0,1)a$ and $\boldsymbol{a}_1+\boldsymbol{a}_2=(\sqrt{3},0)a$ give $(\boldsymbol{b}_1-\mathbf{b}_2)/2=(0,1)2\pi/a$ and $(\boldsymbol{b}_1+\boldsymbol{b}_2)/2=(1/\sqrt{3},0)2\pi/a$, respectively.
[54] S. Piscanec, M. Lazzeri, F. Mauri, A. C. Ferrari, J. Robertson, Phys. Rev. Lett. **93**, 185503 (2004).
[55] E. B. Wilson, Jr., Phys. Rev. **45**, 706 (1934).
[56] E. B. Wilson, Jr., J. C. Decius, and P. C. Cross, *Molecular Vibrations* (Dover, New York, 1955).
[57] G. Varsányi, *Assignments for Vibrational Spectra of Benzene Derivatives* (Akadémiai Kiadó, Budapest, 1974).
[58] M. J. Frisch, G. W. Trucks, H. B. Schlegel, G. E. Scuseria, M. A. Robb, J. R. Cheeseman, J. A. Montgomery, Jr., T. Vreven, K. N. Kudin, J. C. Burant, J. M. Millam, S. S. Iyengar, J. Tomasi, V.

Barone, B. Mennucci, M. Cossi, G. Scalmani, N. Rega, G. A. Petersson, H. Nakatsuji, M. Hada, M. Ehara, K. Toyota, R. Fukuda, J. Hasegawa, M. Ishida, T. Nakajima, Y. Honda, O. Kitao, H. Nakai, M. Klene, X. Li, J. E. Knox, H. P. Hratchian, J. B. Cross, V. Bakken, C. Adamo, J. Jaramillo, R. Gomperts, R. E. Stratmann, O. Yazyev, A. J. Austin, R. Cammi, C. Pomelli, J. W. Ochterski, P. Y. Ayala, K. Morokuma, G. A. Voth, P. Salvador, J. J. Dannenberg, V. G. Zakrzewski, S. Dapprich, A. D. Daniels, M. C. Strain, O. Farkas, D. K. Malick, A. D. Rabuck, K. Raghavachari, J. B. Foresman, J. V. Ortiz, Q. Cui, A. G. Baboul, S. Clifford, J. Cioslowski, B. B. Stefanov, G. Liu, A. Liashenko, P. Piskorz, I. Komaromi, R. L. Martin, D. J. Fox, T. Keith, M. A. Al-Laham, C. Y. Peng, A. Nanayakkara, M. Challacombe, P. M. W. Gill, B. Johnson, W. Chen, M. W. Wong, C. Gonzalez, and J. A. Pople, GAUSSIAN 03, Revision D.01, Gaussian, Inc., Wallingford, CT, 2004.

[59] F. Negri, C. Castiglioni, M. Tommasini, and G. Zerbi, J. Phys. Chem. A **106**, 3306 (2002).

[60] R. A. Friedel and G. C. Carlson, J. Phys. Chem. **75**, 1149 (1971).

[61] R. J. Nemanich, G. Lucovsky, and S. A. Solin, Mater. Sci. Eng. **31**, 157 (1977).

[62] F. Tuinstra and J. L. Koenig, J. Chem. Phys. **53**, 1126 (1970).

[63] C. Thomsen and S. Reich, Phys. Rev. Lett. **85**, 5214 (2000).

[64] S. Hony, C. Van Kerckhoven, E. Peeters, A. G. G. M. Tielens, D. M. Hudgins, and L. J. Allamandora, Astron. Astrophys. **370**, 1030 (2001).

[65] Y. Morino and T. Shimanouchi, Pure Appl. Chem. **50**, 1707 (1978).

[66] T. Miyazawa, J. Chem. Phys. **29**, 246 (1958).

[67] H. Shinohara, Y. Yamakita, and K. Ohno, J. Mol. Struct. **442**, 221 (1998).

[68] G. Herzberg, *Electronic Spectra and Electronic Structure of Polyatomic Molecules* (Van Nostrand, New York, 1966).

[69] S. Lowitzer, B. Winkler, and M. Tucker, Phys. Rev. B **73**, 214115 (2006).

[70] S. J. Cyvin, B. N. Cyvin, J. Brunvoll, J. C. Whitmer, P. Klaeboe, J. E. Gustavsen, and Z. Naturforsch, Z. Naturforsch. A **34**, 876 (1979).

[71] B. N. Cyvin, J. Brunvoll, and S. J. Cyvin, J. Mol. Struct. **346**, 21 (1995).